Journal of Materials Chemistry A

Accepted Manuscript

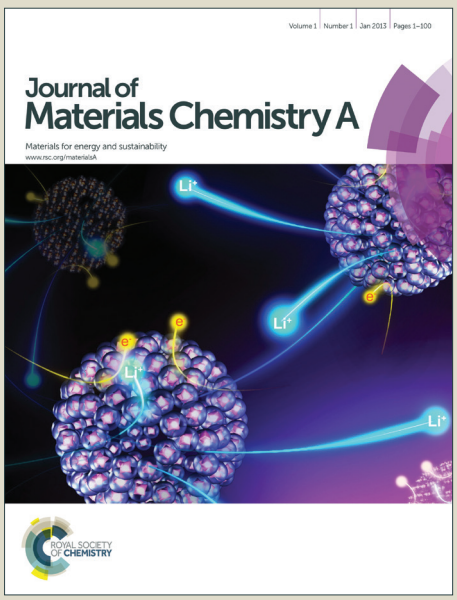

ROYAL SOCIETY OF CHEMISTRY

www.rsc.org/materialsA

A table of contents entry

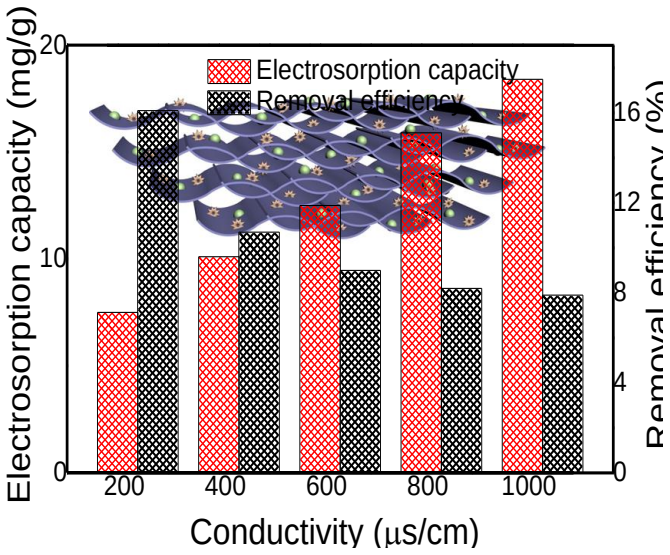

Reduced graphene oxide-polypyrrole-MnO_2 composites are facilely prepared for high performance electrodes for capacitive deionization.

Journal Name

RSCPublishing

ARTICLE

Facile fabrication of graphene-polypyrrole-Mn composites as high performance electrodes for capacitive deionization

Cite this: DOI: 10.1039/xoxxoooooox

Xiaoyu Gu, Yu Yang, Yang Hu, Meng Hu, Jian Huang and Chaoyang Wang*

Received ooth January 2012,
Accepted ooth January 2012

DOI: 10.1039/xoxxoooooox

www.rsc.org/

Three-dimensional reduced graphene oxide-polypyrrole-MnO_2 (RGO-PPy-Mn) composites are facilely prepared by a two-step hydrothermal process. Pyrrole (Py) monomers are polymerized to PPy by $KMnO_4$ in the presence of graphene oxide (GO), then MnO_2 is obtained simultaneously after redox reaction between graphene and $KMnO_4$ to produce RGO-PPy-Mn composites. The influence of mass ratio of Py to GO and mole ratio of $KMnO_4$ to Py on RGO-PPy-Mn composites are investigated. The resultant composites exhibit a hierarchical porous structure with a specific surface area of 331 m^2/g and excellent specific capacity of 356 F/g, much higher than those of pure RGO or PPy electrodes. Enhanced electrochemical capacity and low inner resistance endow RGO-PPy-Mn composite electrodes with outstanding specific electrosorptive capacity of 18.4 mg/g. Furthermore, RGO-PPy-Mn composite electrodes have good rate stability and cycling stability for capacitive deionization applications.

Introduction

Water pollution and contamination have been one of the biggest and most alarming problems because of the rapid development of modern industry. Delivering clean and potable water to the world's people, particularly in developing countries has been a serious challenge. In response to increasing water demand, multiple innovative technologies are considering for seawater desalination to supplement inadequate freshwater source, for example, membrane and thermal separations.[1] However, some defects are still existed in the used systems, such as low efficiency, energy consuming, and secondary pollution.[2] Capacitive deionization (CDI), an electrosorption process to force ionic species toward oppositely charged high-surface-area electrodes under an electric field, is considered as an energy efficient and cost effective desalination technology.[3] It has been developed as a non-polluting and environment-friendly alternative to desalination technologies like reverse osmosis (RO), because its operation requires no pressure, heating or chemical reagent.[4, 5] However, the major issue with the application of CDI to municipal wastewater treatment lies in the scalability and affordability of CDI materials and systems.[6]

Generally, the most widely used materials for electroadsorption devices are carbon-based materials, which store energy using the adsorption of both anions and cations at the electrode-electrolyte interface. With its wide variety of available forms and porosity, carbon has been found to be the electrode material of choice for CDI and other electro-adsorption processes.[7] Among the various forms of carbon investigated for CDI, activated carbon,[8,9] carbon cloth,[10,11] mesoporous carbon,[12-15] carbon fiber,[16,17] carbon nanotubes,[18-22] graphene,[23-25] carbon aerogels[26, 27] and their composites[28,29] have been studied. However, most of those electrode materials were prepared in the laboratory and could hardly meet the large-volume demand by desalination. Recently, graphene and its derivatives have emerged as a key material for designing experimental water treatment strategies owing to their excellent physical, chemical and electronic properties.[30-37] Especially, graphene-based materials can offer high electroactive regions and short diffusion path for the efficient access of the electrolyte to the electrode because of small size and high surface area, which indicate that it is a promising material for electrodes.[38-41]

Recently, the incorporation of conducting polymers and transition metal oxide in some graphene-based materials to improve their capacitance has been remarkably investigated.[42-44] Among conducting polymers, polypyrrole (PPy) are well studied owing to its high electrical conductivity, easy synthetic procedure and cost effectiveness. PPy in the nanoscale exhibits uniquely electrical and electrochemical properties, which allows its application in fabrication of various types of devices.[43] Some researchers have focused on the incorporation of graphene with PPy to produce nanohybrids for supercapacitor electrodes.[45] Because in the novel architectures with conducting polymer, graphene not only serves as a highly conductive support material, but also provides a large surface

for the dispersion of nanoscale PPy. Additionally, the introducing PPy can minimize the restacking effects of graphene sheets as " spacers", thus the electrochemical performance of these composites are enhanced in some degree accordingly.[46] Among transition metal oxides, MnO_2 has stood out due to its outstanding characteristics such as high theoretical specific capacitance (1,400 F/g), natural abundance, and environmental friendliness.[47] Various methods have been used to prepare MnO_2/carbon composites, including physical mixing,[48] thermal decomposition,[49] ball milling,[50] electrodeposition[51] and redox reaction. Furthermore, the reduction of aqueous permanganate by surface carbon to insoluble manganese oxide, depositing simultaneously as a thin film on the carbon surface is most attractive in all these methods.[52] Ternary composite electrodes, combining graphene, conducting polymers and transition metal oxides have been explored because of their synergistic properties.

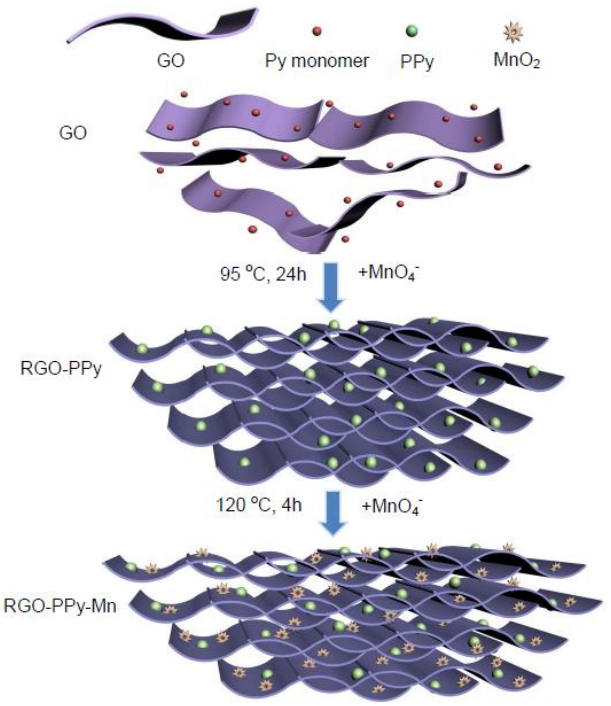

Fig. 1 Schematic illustration for the synthesis of RGO-PPy-Mn composite.

Here, we developed a three-dimensional (3D), hierarchically porous, reduced graphene oxides-polypyrrole-MnO_2 (RGO-PPy-Mn) composites with large specific surface area and high specific capacitance, which was deposited of two active materials (PPy and MnO_2) into the graphene network (**Fig. 1**). During the first hydrothermal process of the composite hydrogels, graphene oxides (GO) was thermally reduced into graphene and aggregated to RGO hydrogels, meanwhile pyrrole (Py) were oxidized to PPy by $KMnO_4$ at the same time; then MnO_2 were obtained after redox reactions between graphene and $KMnO_4$ in the next hydrothermal process. On the one hand, the RGO-PPy-Mn hydrogels have a well-defined 3D porous network, which offers an opportunity to optimize the ionic diffusion in graphene-based electrodes for electrical double-layer capacitance (EDLC). On the other hand, the synergistic effect from a combination of PPy and MnO_2 resulted to the improved capacitive properties and enhanced ion transportation in comparison with the pristine RGO and PPy electrodes.[53] We also prepared RGO-PPy-Cu hydrogels with Cu^{2+} as an oxidant to demonstrate the advantage of MnO_2 in the RGO-PPy-Mn hydrogels.[54] The as-prepared RGO-PPy-Mn electrodes show enhanced specific capacitance in electrochemical performance and outstanding specific electrosorptive capacity in CDI performance, indicating that RGO-PPy-Mn electrode is quite appropriate for high performance and low energy consumption capacitive deionization.

Experimental section

Reagents and chemicals

Natural graphite powder and pyrrole (Py) were purchased from J&K Scientific Ltd. (China). All other reagents were purchased from Guangzhou Chemical Reagent Co. (China) and used without further purification. Water used in all experiments was deionized and filtrated by a Millipore purification apparatus with resistivity more than 18.0 MΩ·cm.

Preparation of RGO-PPy-Mn composites

GO was prepared from purified natural graphite via the modified Hummer's method and the corresponding details can be obtained in our previous report.[55] GO solution of 4 mg/mL was obtained after the product was ultrasonicated for 2 h in deionized water. Then Py aqueous solution (40 mg/mL) and $KMnO_4$ solution (1 M) were added into GO dispersion and ultrasonicated for 30 min. The Py/GO mass ratio was set to vary from 0.5:1 to 2:1, and the $KMnO_4$/Py mole ratio was changed from 0.2:1 to 0.8:1.[53] Then the above mixtures were heated to 95 ^oC for over 12 h to form the RGO hydrogels, meanwhile Py monomers were polymerized to PPy.[56,57] The obtained RGO-PPy hydrogel was immersed in the $KMnO_4$ solution (0.2 M), and then transferred into a Teflon-lined stainless steel autoclave, sealed and maintained at 120 ^oC for 4 h.[58] Finally, the resulting hydrogel was rinsed with distilled water and then freeze-dried by a vacuum freeze dryer to maintain the porous structure. For convenience, the samples are denoted by RGO-PPy_a-Mn_b, where subscript a represents the mass ratio of Py to graphene and subscript b represents the mole ratio of $KMnO_4$ to Py. For comparison, RGO-PPy_a-Cu_b hydrogels were prepared in the same route using $CuSO_4$ instead of $KMnO_4$, where subscript a represents the mass ratio of Py to GO and subscript b represents the mole ratio of $CuSO_4$ to Py.[59] RGO hydrogel and PPy nanoparticles were also prepared according to the above procedures in the absence of Py and GO, respectively.

Electrochemical measurements

The working electrode was prepared by pressing a piece of RGO-PPy-Mn hydrogel onto a nickel foam plate. The electrodes were dried at room temperature overnight before

investigation of the electrochemical performance of the electrodes. A three-electrode cell system, including graphene-based electrode, Pt foil and Ag/AgCl (3M KCl) were used as the working, counter and reference electrodes. All of the experiments were carried out in 1M NaCl aqueous electrolyte.

Cyclic voltammetry (CV) analysis of graphene-based electrodes was measured using an electrochemical workstation (CHI660C instruments, Shanghai, China). The potential range for CV was -1.0-0 V and the effects of changes in the scan rate were examined by supplying 5, 10, 20 and 50 mV/s.

The galvanostatic charge/discharge (GC) tests were conducted on an automatic LAND battery test instrument (CT2001A) to evaluate the charge-discharge performance in 1M NaCl aqueous solution. Here, the specific capacitances Cs were calculated from the slope of discharge curves by using the following equation:

$$C_s = \frac{I\Delta t}{m\Delta V} \quad (1)$$

where Cs (F/g) is the specific capacitance, I (A) is the constant discharge current, Δt (s) is the discharging time, m (g) is the mass of working electrode in milligram scale, ΔV is the voltage drop upon discharging (excluding the iR drop).

Electrochemical impedance spectroscopy (EIS) measurements were also measured by CHI 660C. The amplitude of the alternating voltage was 5 mV around the equilibrium potential (0 V) and the data was collected in the frequency range from 100 mHz to 100 kHz.

In addition, the specific power and specific energy were calculated according to Eq. 2 and 3, respectively, as follows:[60]

$$E = \frac{I \times V \times t}{m} \quad (2)$$

$$P = \frac{I \times V}{m} \quad (3)$$

where E is the specific energy; P is the specific power; I is the discharge current; V is the voltage excluding the IR drop; t is time in hours and m is the mass of the electrodes.

Electrosorptive capacity measurement

Graphite papers were used as inert current collectors on the back sides of the electrodes, and the working electrodes were prepared in the same manner as above in electrochemical measurements. The size of the electrode was 50 × 50 mm and each electrode mass was 0.2 g. A flow channel was created by punching a 1 cm diameter hole in the graphite sheet so that the solution could be in contact with all sides of the working electrodes and could run through the spacer to the outer reservoir (Fig. S1). The electrosorptive capacity of the graphene-based electrode was conducted in a recirculating system including an electrosorptive unit cell, a reservoir, a peristaltic pump (BT-100), and a conductivity meter. Details of the apparatus and experimental procedures can be found in other studies.[61] A given potential was applied to the CDI cell using a potentiostat (RS1302DQ). The conductivity of the effluent water was measured by connecting a conductivity meter (DDS 307) at the position where the solution exited the cell. NaCl solution with an initial conductivity in a total volume of 200 mL was continuously pumped into the unit cell by a peristaltic pump with a flow rate of 10 mL/min to the feed tank. The relationship between conductivity and concentration of NaCl solution can be found in Fig. S2. Herein, the electrosorptive capacity (q_e, mg/g) of current electrodes is calculated according to the following equation:[62]

$$q_e = \frac{(C_0 - C_e)V}{m} \quad (4)$$

where C_0 (mg/mL) and C_e (mg/mL) are the initial and equilibrated NaCl concentrations, respectively; V (mL) is the volume of the container and m (g) is the mass of active components in two working electrodes.

Characterization

The morphology of RGO-PPy-Mn hydrogels were examined by scanning electron microscopy (SEM Zeiss EVO18) operating at 10 KV and PPy nanoparticles were observed by field emission scanning electron microscopy (FESEM NOVA NANOSEM 430), all samples were sputter-coated with a thin overlayer of gold to prevent sample charging effects. The X-ray diffraction (XRD) pattern of PPy nanoparticles and RGO-PPy composites were obtained using an X'pert PRO diffractometer (40 kV and 40 mA) equipped with a Cu Kα radiation (wavelength 0.154 nm) at room temperature. FT-IR spectra were obtained on FT-IR NICOLET 6700 spectrometer at a nominal resolution of 2 cm^{-1}. Theta Probe X-ray Photoelectron Spectroscopy (XPS, ESCA Axis Ultra DLD) was used to verify the valence state of carbon and nitrogen. The Brunauer-Emmett-Teller (BET) method was utilized to calculate the specific surface area. The pore size distributions were derived from desorption branch by using the Barrett-Joyner-Halenda (BJH) model. Before the measurements, all samples were degassed overnight at 373 K in a vacuum line.

Results and discussion

Fabrication of RGO-PPy-Mn composites

We prepared RGO-PPy-Mn hydrogels in two hydrothermal steps and the participation of $KMnO_4$ played a key role in the fabrication of RGO-PPy-Mn hydrogels. First, $KMnO_4$ as an oxidant was used to polymerized Py monomers to PPy under heating condition, meanwhile GO were reduced to RGO hydrogel with a 3D porous structure; then MnO_2 was obtained after the redox reaction between graphene and $KMnO_4$ during hydrothermal process.[63] Detailed preparation process of RGO-PPy-Mn composites is shown in Fig. 1.

An effective formation of RGO-PPy-Mn composites was revealed by XRD and FT-IR. **Fig. 2** is XRD patterns and FT-IR spectra of GO, RGO, PPy, RGO-PPy$_{0.5}$-Cu$_1$ and RGO-PPy$_{0.5}$-Mn$_{0.4}$. As shown in Fig. 2a, RGO sheets exhibited a strong intense (002) peak at 2θ=25° and the (001) peak of GO at 10.3° disappeared, indicating that most of the oxygen-containing groups on basal planes of the carbon networks had been removed. However, no clear peaks can be found in PPy nanoparticles because of a poorly crystallized structure and approximately amorphous nature of the PPy powder. For the RGO-PPy-Cu hybrid hydrogels, the peaks at 25° decreased after the addition of PPy nanoparticles, which also confirmed that PPy nanoparticles were uniformly distributed in RGO sheets. Compared with RGO-PPy-Cu composites, four peaks at 2θ around 25°, 37°, 41° and 51° appeared in RGO-PPy$_{0.5}$-Mn$_{0.4}$ hybrid hydrogels, which can be indexed to potassium manganese oxide hydrate MnO_2 (JCPDS 42-1317).[52] Additionally, the peak at 2θ around 25° became sharp after the deposition of MnO_2, indicating that the surfaces of graphene were deposited by nanoscale MnO_2, resulting in the low degree of graphitization.

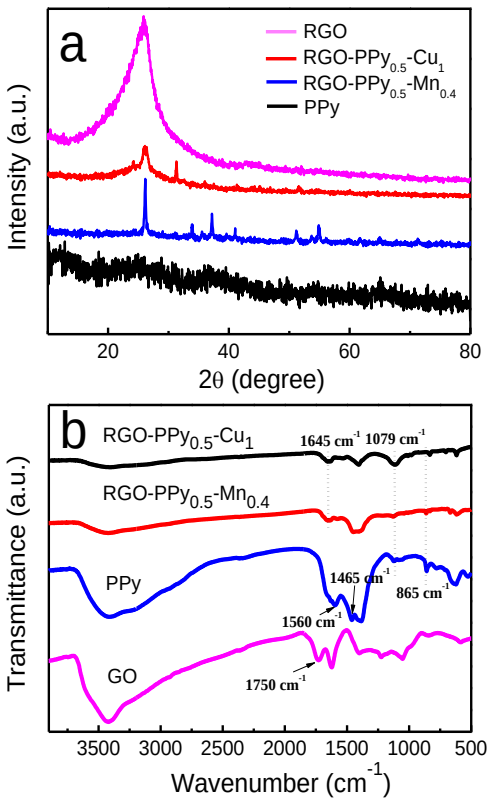

Fig. 2 (a) XRD patterns and (b) FT-IR spectra of composites.

The FT-IR technique was also used to track the process of preparation of RGO-PPy-Mn ternary composites. From Fig. 2b, the peaks located at 3400 and 1750 cm^{-1} were corresponded to the -OH and C=O functional groups in GO, but they cannot be found in RGO-PPy-Mn and RGO-PPy-Cu hybrid hydrogels, which shows that GO has been chemically reduced to RGO via the hydrothermal method. After polymerizing PPy onto the sheets of the RGO, the peaks at 1465 and 1645 cm^{-1} which are assigned to C-N stretching vibration and antisymmetric ring-stretching, the N=Q=N (quinoid, Q) at 1079 cm^{-1}, γ(C-H) of the 1,4-disubstituted aromatic ring at 865 cm^{-1} were observed.[64] The FT-IR spectrum of RGO-PPy-Mn shows two significant peaks at 607 and 528 cm^{-1} (Fig. S3), which corresponds to the coupling between the Mn-O stretching modes of tetrahedral and octahedral sites, respectively.[65] Due to the clear presence of the vibrational peaks corresponding to PPy and the complete disappearance of the peaks assigned to GO, along with the XRD patterns, it can be safely concluded that the RGO-PPy-Mn ternary composites have been successfully prepared.

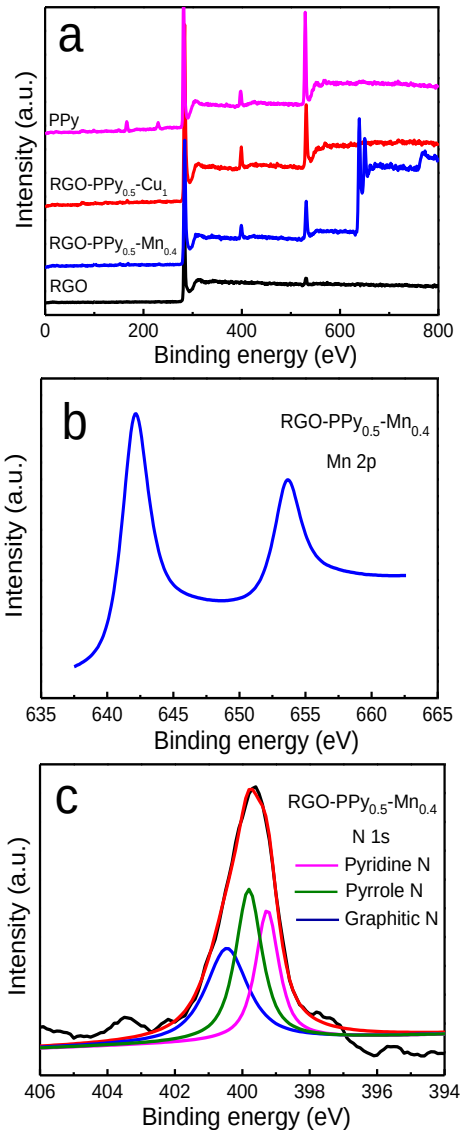

Fig. 3 (a) Wide survey scans of the XPS spectra of composites. XPS spectra of (b) Mn 2p peaks and (c) N 1s peaks of RGO-PPy$_{0.5}$-Mn$_{0.4}$ composite.

Surface elemental analysis was carried out by XPS on the RGO, PPy, RGO-PPy-Mn, and RGO-PPy-Cu composites. Wide survey scans of the XPS spectra of RGO-PPy-Mn composites revealed signals from Mn, O, N, and C elements, while no Mn signals can be observed from other three samples (**Fig. 3**a).

Obviously in Fig. 3a, there was only a C1s peak and very weak O1s peak of RGO. From the XPS C1s core level spectra of RGO in Fig. S4, the intensities of all the peaks of oxygen functional groups in RGO were decreased and the intensity of the Csp^2 peak was increased simultaneously, indicating that most of the oxygen groups have been removed. The O1s peaks of others were stronger because of the introduction of PPy and MnO_2. Similarly, we observed Mn 2p peak and N1s peak in RGO-$PPy_{0.5}$-$Mn_{0.4}$ composites. In Fig. 3b, a 2p3/2-2p1/2 doublet at 650.9 and 639.5 eV is shown in the Mn 2p region, and the splitting width is 11.4eV, indicating Mn^{4+} ions are the main components of the manganese element. The N1s spectra of RGO-$PPy_{0.5}$-$Mn_{0.4}$ composites can be fitted into three peaks at 398.2, 399.7 and 401.3 eV (Fig. 3c). The peaks with lower binding energy located at about 398.2 and 399.7 eV corresponded to pyridine-like (C=N-C) and pyrrole-like (N-$(C)_3$) nitrogen, while the peak 401.3 eV corresponded to the quaternary nitrogen.[66]

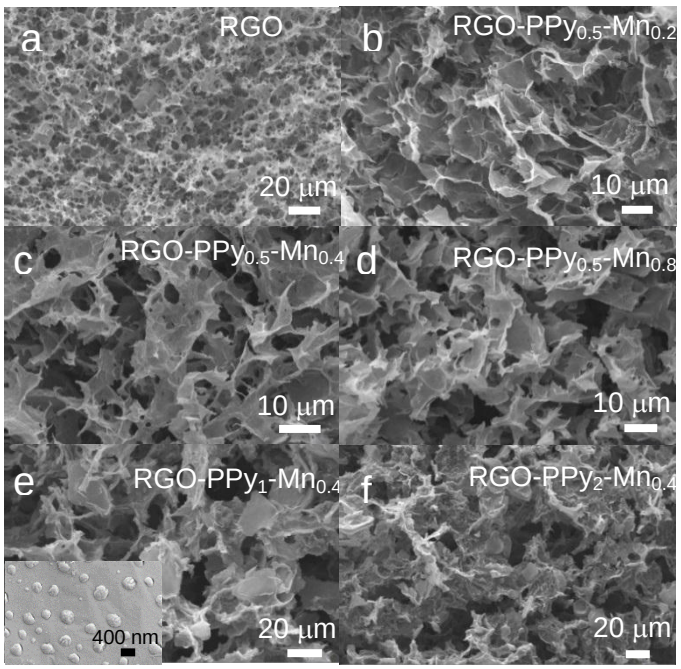

Fig. 4 SEM images of (a) RGO and (b-f) RGO-PPy-Mn composites. The inset in e is high magnification image of RGO-PPy_1-$Mn_{0.4}$ composite.

The morphology and structure of RGO, PPy and RGO-PPy-Mn hydrogels with different parameters were observed by SEM and FESEM. From SEM images in **Fig. 4**, all the RGO and RGO-PPy-Mn hybrid hydrogels exhibited typical cross-linked 3D network feature with interconnected pores of sub-micrometers to several micrometer, the walls of the pores consisted flexible graphene nanosheets.[54] Such porosities facilitated the transport of electrons and ions during the charge–discharge process, thus provided great promise in preparing self-supported and binder-free graphene-based EDLC electrodes.[67] Furthermore, the well preserved 3D network of RGO can effectively prevent the agglomeration and restacking of both graphene and PPy, which leaded to an enhanced electrical double-layer capacitance.[53] Additionally, the pores in the RGO hydrogel were a few micrometers in size, much smaller than that of RGO-PPy-Mn hydrogels. As shown in Fig. S5, the RGO-PPy-Mn hydrogel had 3 times a volume of that formed from normal pyrrole-free GO suspension under the same condition. The existence of Py will effectively prevent the self-stacked behavior of GO during hydrothermal process, and accordingly increase the available GO sheets for forming large volume of 3D graphene hydrogel.[68] It is because the Py monomer can easily attach on the surfaces of GO sheets through H-bonding or π-π interaction owing to a typical conjugated structure with electron-rich N atom. Additionally, **Fig.** S6 is SEM image and C-, O- and Mn- elemental mappings for RGO-PPy-Mn composites. Nitrogen and manganese elements were uniformly distributed in RGO-PPy-Mn composites, providing an evidence for the successful PPy and manganese incorporation.

The effect of mass ratio of Py to graphene was also analyzed because uniform and thin coating of graphene by PPy was a basic condition to achieve better capacitance properties. As shown in Fig. 4c,e,f of SEM images of RGO-PPy_a-$Mn_{0.4}$ (a=0.5, 1, 2) hybrid hydrogels, the 3D porous structure was maintained well with a slightly increased wall thickness due to the PPy mixing increase. When the mass amount of Py was less than graphene, the majority of Py were polymerized onto the graphene sheets. As shown the inset image of RGO-PPy_1-$Mn_{0.4}$ in Fig. 4e, a few nanoparticles with a diameter of 300 nm uniformly distributed on the RGO sheets of RGO-PPy_1-$Mn_{0.4}$ hybrid composites. As we know, the diameter of pure PPy nanoparticles polymerized by $KMnO_4$ was about 300 nm (Fig. S7). Therefore it confirmed that PPy nanoparticles were uniformly distributed onto the graphene sheets of RGO-PPy_1-$Mn_{0.4}$. However, when the mass ratio of Py to GO exceeded 1:1, polymerization of Py outside the graphene surface also occurred, which resulted to the clusters of pure PPy domains. As shown in Fig. 4f, a thick coating of PPy onto the graphene sheets was observed for the RGO-PPy_2-$Mn_{0.4}$ hydrogels, along with decrease of porosity amount and pore diameter. This may be because higher amount of pyrrole would promote the formation of PPy on the graphene surface and resulted in a thick coating and PPy aggregation.[69] So we can confirm that the uniform polymerization of Py by MnO_4^- along graphene sheets were successfully prepared in this work. In addition, the hydrophilicity of the electrode has a great effect on solvent accessible area.[19] As shown in Fig. S8b, the contact angle of the RGO-PPy-Mn electrode was about 45 °, while the contact angle of the RGO electrode was 66 ° (**Fig.** S8a). The slightly high wettability of the RGO-PPy-Mn electrode was from the hydrophilicity of PPy and MnO_2, which significantly increased the solvent accessible area and the diffusion rate of the electrolyte. Therefore, RGO-PPy-Mn electrodes would have a higher efficient removal of NaCl compare with the graphene electrode with a low wettability because of the hydrophobicity of the carbon surface.[70]

The pore structure arrangement of the prepared samples was further investigated by a nitrogen adsorption-desorption

measurement. The BET surface area, pore volumes, and average pore size of all samples are shown in Table S1. As exhibited in **Fig. 5**, the profile of all samples show a representative type-IV isotherm, together with a H_3-type hysteresis hoop in a wide relative pressure (P/P_0) of 0.2-0.85, which indicates the mesoporous characteristic of the solid material.[71] The BET specific surface area of RGO-$PPy_{0.5}$-$Mn_{0.4}$ was measured to be 331 m^2/g (Fig. 5b), which was much higher than that of RGO (120 m^2/g, Fig. 5a) and PPy (63 m^2/g, Fig. 5c). Compared to that of RGO and PPy, the hysteresis hoop area of RGO-$PPy_{0.5}$-$Mn_{0.4}$ was considerably enlarged, which further confirmed that the incorporation of PPy nanoparticles and MnO_2 effectively prevented the aggregation of individual graphene sheets during reduction. Additionally, RGO-$PPy_{0.5}$-Cu_1 had a specific surface area (SSA) of 144 m^2/g (Fig. S9), which is smaller than that of RGO-$PPy_{0.5}$-$Mn_{0.4}$, but larger than that of RGO.

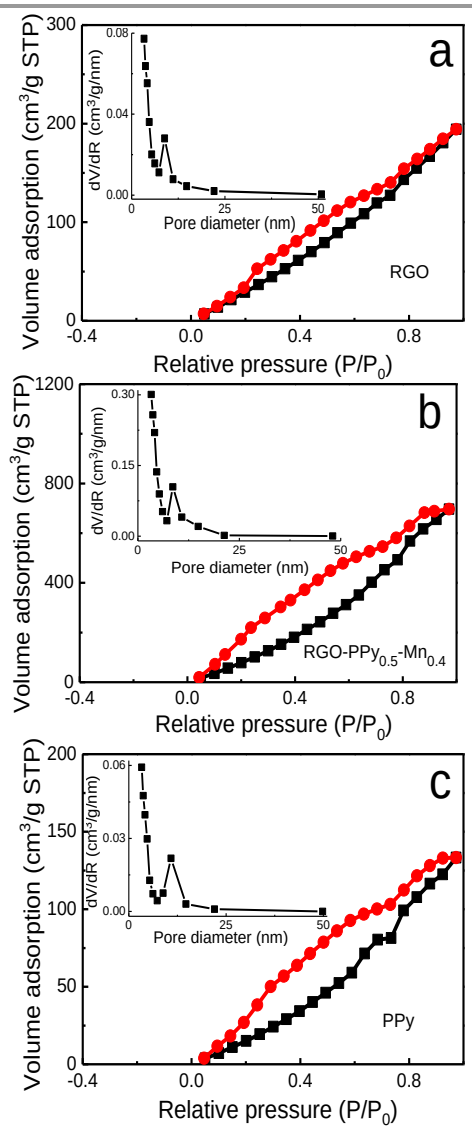

Fig. 5 Nitrogen sorption isotherms and pore size distribution (inset) of (a) RGO, (b) RGO-$PPy_{0.5}$-$Mn_{0.4}$, and (c) PPy.

Electrochemical performance

In order to analyze the electrochemical properties of the prepared electrodes, CV measurements, GC and EIS technique which are strongly sensitive to the capacitive characteristics of carbon electrodes for adsorption/desorption capacity were used in three electrode system to evaluate the electrosorption ability of RGO-PPy-Mn composites. **Fig. 6**a exhibited the CV spectra of the RGO-PPy-Mn electrodes with a potential range between -1 and 0 V. We can find that the CV curves of RGO-PPy-Mn electrodes deviated from rectangular shape due to the content of PPy and MnO_2. Obviously, the CV enclosed area for RGO-$PPy_{0.5}$-$Mn_{0.4}$ is larger than other two composites, demonstrating a much higher capacitance, which can also be confirmed by their GC curves in Fig. 6b. According to Eq. 1, the Cs of RGO-$PPy_{0.5}$-$Mn_{0.4}$ is 356 F/g, larger than others because of the longer discharge time. This implies that the more addition of $KMnO_4$ may lead to faster reaction speed or an increase in thickness of polymer PPy, but the condensed packing will result in surface area overlap of PPy. As shown in Fig. 6b, the GC curves of all electrodes displayed symmetric and linear shapes with a low potential drop. **Fig. S10a** showed that iR drop was about 0.06V, indicating that RGO-PPy-Mn electrodes exhibited good stability in repeat charge–discharge processes. Comparative CV profiles of the RGO-$PPy_{0.5}$-$Mn_{0.4}$ electrodes at various scan rates are displayed in Fig. 6c. When the scanning rate increased from 5 to 50 mV/s, the shape of the CV curves showed an increased distortion from the typical rectangular shape. Also, the specific capacitance decreased with the increased scanning rate, which can be attributed to the greater charge mobilization per unit time. The effect of different mass ratios of Py to graphene in electrochemical properties has been studied, as shown in Fig. 6d. Among different ratios of Py to graphene, RGO-$PPy_{0.5}$-$Mn_{0.4}$ has the largest Cs value, especially much larger than RGO-PPy_2-$Mn_{0.4}$. As shown in the inset of Fig. 4e, aggregation of PPy were formed on the surface of RGO-PPy_2-$Mn_{0.4}$, which can restrict the access of electrolyte to the surface of graphene and therefore decrease the effective surface area of the electrode and the capacitance.[69] Fig. S10b shows the Nyquist plots of the EIS spectra for the RGO-PPy_a-$Mn_{0.4}$ (a=0.5, 1, 2) electrodes. We can find that the slope of RGO-PPy_2-$Mn_{0.4}$ was larger than other two, which means larger Warburg resistances were observed for it. Hence, RGO-PPy-Mn composites worked better in electrochemical performance when the mass amount of Py was smaller than graphene.

From the CV curves in Fig. 6e, it is obvious that the current density of the RGO-PPy-Mn composite electrodes is much higher than that of the RGO-PPy-Cu and RGO electrodes. For comparison with RGO-PPy-Mn hydrogels, CV analysis of as-prepared RGO-PPy-Cu composites is depicted in Fig. S10c. As we see, RGO-PPy-Cu electrodes had the similar CV curves to that of RGO-PPy-Mn electrodes. However, different from manganese ion, the valence state of Cu^{2+} cannot change during hydrothermal process and no benefit would CuO offer to the capacitive properties of RGO-PPy-Cu composites. The higher

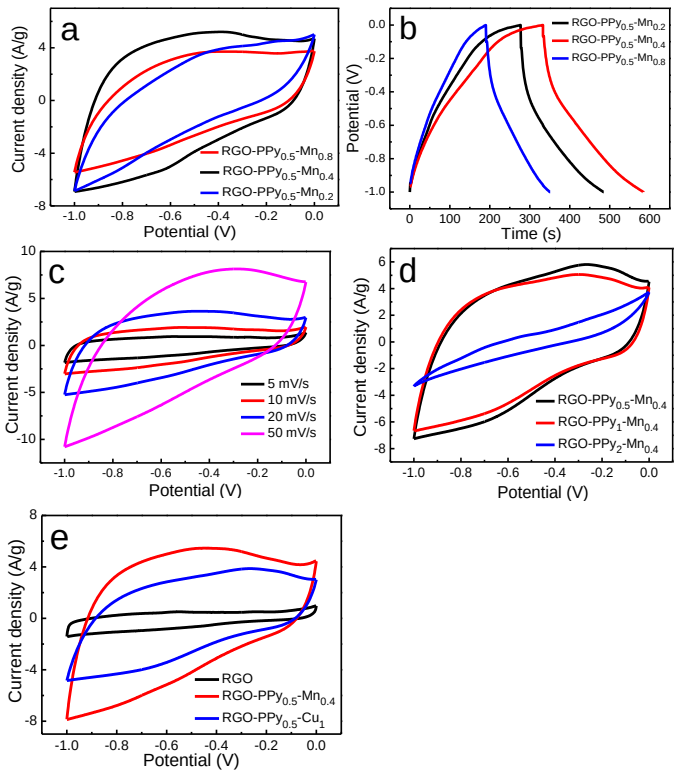

Fig. 6 (a) CV curves at a scan rate of 10 mV/s and (b) GC curves at a current of 1 A/g of RGO-$PPy_{0.5}$-Mn_b (b = 0.2, 0.4, 0.8) electrodes. (c) CV curves of RGO-$PPy_{0.5}$-$Mn_{0.4}$ electrode at various scan rates. (d) CV curves of RGO-PPy_a-$Mn_{0.4}$ (a = 0.5, 1, 2) electrodes at a scan rate of 10 mV/s. (e) CV curves of RGO, RGO-$PPy_{0.5}$-Cu_1 and RGO-$PPy_{0.5}$-$Mn_{0.4}$ electrodes at a scan rate of 10 mV/s.

specific capacitance of the RGO-PPy-Mn electrodes can be ascribed to the fabrication of a hybrid capacitor for charge storage and enhanced electrochemical properties.[72] The key to the high performance of this hybrid is the addition of $KMnO_4$: (1) Py was polymerized by MnO_4^- as well as the reduction of GO in the first reaction. Compared with RGO, the conductivity of RGO-PPy-Mn increased due to the the high conductivity of PPy and the bridge function of RGO for the electronic hopping between PPy chains.[64] The electrical conductivity of RGO-PPy-Mn electrode was 24 S/m, which was much bigger than that of RGO electrode (0.34 S/m) from the conductivity tests. (2) The carbon substrate served as a sacrificial reductant and converted aqueous permanganate (MnO_4^-) to insoluble MnO_2, which in turn, deposited on the surfaces of graphene and PPy.[63] Except the RGO and PPy, MnO_2 nanoparticles also had the potential to enhance the energy density through optimizing the ionic diffusion in graphene sheets, which can enhance the overall capacitance of the RGO-PPy-Mn composites. (3) Additionally, the poor electrical conductivity of MnO_2 (10^{-5}-10^{-6} S/cm) always limited itself to achieve theoretical specific capacitance.[73] PPy served as nanostructured scaffolds for electron transporting between MnO_2 and graphene, which provided an efficient strategy for overcoming the low conductivity of MnO_2. In conclusion, the RGO-PPy-Mn composites exhibited improved capacitive properties and enhanced ion transportation in comparison with the pristine RGO because of the synergistic effect of the high capacitance of PPy and MnO_2 coating and the porous structure of RGO network.[74-76]

CDI performance

With the self-made batch mode desalination apparatus depicted in Fig. S1, the desalination behaviours and regeneration performances of RGO-PPY-Mn, RGO-PPy-Cu, RGO and PPy electrodes were measured under 2.0 V with an initial conductivity of 1000 μS/cm, and the resultant profiles are exhibited in **Fig. 7**a. The potential difference given herein exceeded the 1.23 V threshold to compensate for the circuit system resistance. When the applied voltage was 1.2 V, the conductivity did not decrease with time, indicating that 1.2 V is not big enough to absorb NaCl from the solution.[77] However, even when the applied voltage was at 2.0 V, no visible gas bubbles were observed, indicating that no water electrolysis was taking place. Therefore, all CDI tests herein were carried under 2.0 V.[78] As we can see, the conductivity of all electrodes decreased dramatically at the initial stage, which demonstrated quick adsorption of the salt ions by oppositely charged carbon electrode. As time went on, the conductivity decreased slowly and tended to be a constant value, because the electrostatic repulsion between the adsorbed ions prevented the constancy of electrosorption.[62] According to Eq. 4, the electrosorptive capacity of 18.4 mg/g for RGO-PPy-Mn was obtained, much higher than 15.1, 9.2, 4.8 mg/g for RGO-PPy-Cu, PPy, and RGO, respectively. The enhanced salt removal performance can be attributed to the improved nanostructure and electrochemical properties. Due to its high surface area, graphene can enhance the interaction between PPy, MnO_2 and electrolyte, and hence facilitate the electric double layer generation. Furthermore, after depositing active materials onto graphene sheets, more electrochemically active sites will be used during charge-discharge process, resulting in a much higher electrosorption capacity for CDI electrodes.[73, 75]

The electrosorptive capacities of RGO-PPy-Mn electrode with different initial concentration were measured to investigate the effect of ion concentration on its CDI performance. As shown in Fig. 7b, the total capacity increased but salt removal efficiency decreased as the ion solution concentration was increased. The electrosorptive capacities were 7.5, 10.1, 12.5, 15.9, 18.4 mg/g as the initial concentrations of the NaCl solutions were 200, 400, 600, 800, 1000 μs/cm, whereas the salt removal efficiency were 16.1, 10.7, 9, 8.2, and 7.9 %, respectively. The electrosorptive capacities increased because of the overlapping effect of the electrical double layer on the micropores decreased in ionic resistance at higher salt concentrations.[79] However, removal efficiency decreased as the amount of salt freshly introduced into the system was much greater than that removed from the system. In general, with a lower concentration, the electric field can extend to a longer distance since the solution was less effective in holding the charge. Therefore, it suggests that CDI is envisioned to be a very energy efficient water desalination technology when the ionic content is relatively low.[80]

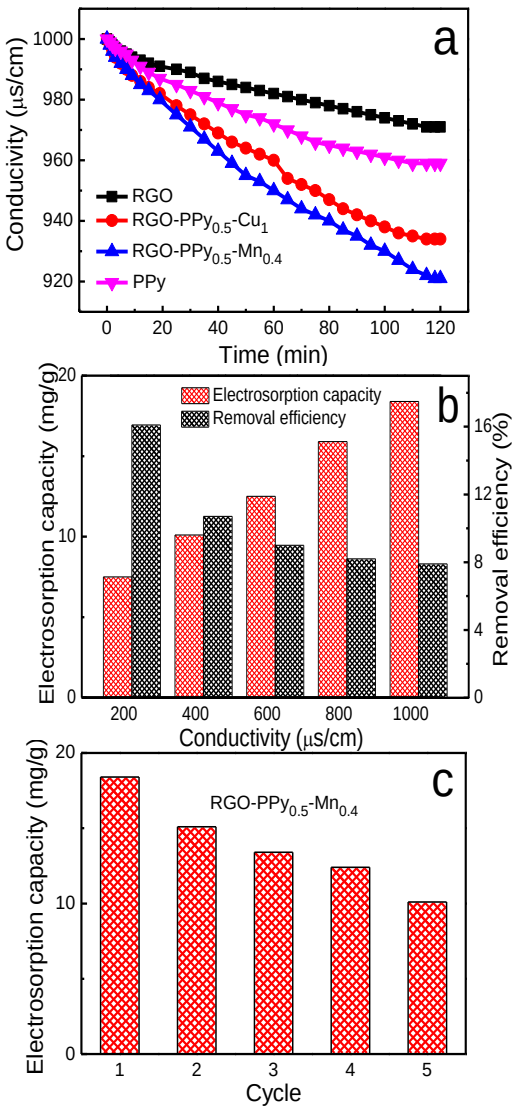

Fig. 7 (a) CDI profiles of RGO, RGO-$PPy_{0.5}$-Cu_1, RGO-$PPy_{0.5}$-$Mn_{0.4}$, and PPy electrodes under 2.0 V. (b) Electrosorption capacity and removal efficiency of RGO-$PPy_{0.5}$-$Mn_{0.4}$ electrode in NaCl solutions with respect to different initial concentrations. (c) Regenerated electrosorptive capacity of RGO-$PPy_{0.5}$-$Mn_{0.4}$ electrode.

After the electrode reached their adsorption capacity, a discharge cycle was initiated by turn off the cell voltage to test the reversibility and stability of the RGO-PPy-Mn electrode. Fig. 7c shows the regenerated electrosorptive capacity of RGO-$PPy_{0.5}$-$Mn_{0.4}$ electrodes, and the electrosorptive capacities are 18.4, 15.1, 13.4, 12.4 and 10.1 mg/g from the first to fifth time. It was also noted that RGO-PPy-Mn electrodes could be regenerated by a simple short circuit without the reversal charge, confirming that the CDI could be regenerated very well without any driving energy and secondary pollution which is critical for large scale application.[80] These CDI results further establish that the RGO-PPy-Mn composite offers greater promise than graphene or PPy as a cost effective, low-energy demand material for CDI applications.

Conclusions

We have developed a 3D porous RGO-PPy-Mn electrode with two active materials (PPy and MnO_2) deposited into the graphene network, combining the hydrothermal method with the chemical oxidative polymerization, in which $KMnO_4$ played a key role. The synergistic effect from a combination of PPy and MnO_2 plus the porous conductive graphene network offered RGO-PPy-Mn electrodes excellent microstructure and morphological properties. The enhanced electrochemical properties of the 3D RGO-MF electrodes leaded to an outstanding specific electrosorptive capacity of 18.4 mg/g, which was much higher than pure RGO and PPy electrodes. Therefore, the obtained RGO-PPy-Mn ternary composites are expected to be promising electrode materials to design high-performance CDI devices.

Acknowledgements

This work was financially supported by the National Natural Science Foundation of China (21274046 and 21474032) the National Natural Basic Research Program of China (973 Program, 2012CB821500) and the Natural Science Foundation of Guangdong Province (S2012020011057).

Notes and references

Research Institute of Materials Science, South China University of Technology, Guangzhou 510640, China. Fax & Tel: +86-20-22236269; E-mail: zhywang@scut.edu.cn

† Electronic Supplementary Information (ESI) available: Schematic illustration of single CDI device, SEM images of PPy nanoparticles, XPS C1s spectrum of RGO, Nitrogen sorption isotherm of RGO-$PPy_{0.5}$-Cu_1, Nyquist plots of the EIS for RGO-PPy-Mn electrodes and CV curves of RGO-PPy-Cu electrodes. See DOI: 10.1039/b000000x/

1. A. Subramani, M. Badruzzaman, J. Oppenheimer and J. G. Jacangelo, *Water Res.*, 2011, **45**, 1907.
2. M. A. Anderson, A. L. Cudero and J. Palma, *Electrochim. Acta*, 2010, **55**, 3845.
3. Y. Oren, *Desalination*, 2008, **228**, 10.
4. C. Tsouris, R. Mayes, J. Kiggans, K. Sharma, S. Yiacoumi, D. DePaoli and S. Dai, *Environ. Sci. Technol.*, 2011, **45**, 10243.
5. F. A. AlMarzooqi, A. A. Al Ghaferi, I. Saadat and N. Hilal, *Desalination*, 2014, **342**, 3.
6. P. Liang, L. Yuan, X. Yang, S. Zhou and X. Huang, *Water Res.*, 2013, **47**, 2523.
7. D. R. Dreyer, S. Park, C. W. Bielawski and R. S. Ruoff, *Chem. Soc. Rev.*, 2010, **39**, 228.
8. R. T. Mayes, C. Tsouris, J. O. Kiggans Jr, S. M. Mahurin, D. W. DePaoli and S. Dai, *J. Mater. Chem.*, 2010, **20**, 8674.
9. S. J. Yang, T. Kim, K. Lee, Y. S. Kim, J. Yoon and C. R. Park, *Carbon*, 2014, **71**, 294.
10. J. Y. Lee, S. J. Seo, S. H. Yun and S. H. Moon, *Water Res.*, 2011, **45**, 5375.
11. M. W. Ryoo, J. H. Kim and G. Seo, *J. Colloid. Interface. Sci.*, 2003, **264**, 414.
12. T. Y. Ma, L. Liu and Z. Y. Yuan, *Chem. Soc. Rev.*, 2013, **42**, 3977.
13. M. Oschatz, L. Borchardt, M. Thommes, K. A. Cychosz, Y. Gogotsi and S. Kaskel, *Angew. Chem. Int. Ed.*, 2012, **51**, 7577.
14. Z. Peng, D. S. Zhang, L. Y. Shi, T. T. Yan, S. Yuan, H. R. Li, R. H. Gao and J. H. Fang, *J. Phys. Chem. C*, 2011, **115**, 17068.

15. X. R. Wen, D. S. Zhang, L. Y. Shi, T. T. Yan, H. Wang and J. P. Zhang, *J. Mater. Chem.*, 2012, **22**, 23835.
16. H. B. Li, Y. Gao, L. K. Pan, Y. P. Zhang, Y. W. Chen and Z. Sun, *Water Res.*, 2008, **42**, 4923.
17. Z. Y. Lin, Z. Li, K. S. Moon, Y. N. Fang, Y. G. Yao, L. Y. Li and C. P. Wong, *Carbon*, 2013, **63**, 547.
18. J. Benson, I. Kovalenko, S. Boukhalfa, D. Lashmore, M. Sanghadasa and G. Yushin, *Adv. Mater.*, 2013, **25**, 6625.
19. D. S. Zhang, L. Y. Shi, J. H. Fang, K. Dai and J. Q. Liu, *Mater. Chem. Phys.*, 2006, **96**, 140.
20. D. S. Zhang, L. Y. Shi, J. H. Fang and K. Dai, *J. Mater. Sci.*, 2006, **42**, 2471.
21. Z. Peng, D. S. Zhang, T. T. Yan, J. P. Zhang and L. Y. Shi, *Appl. Surf. Sci.*, 2013, **282**, 965.
22. K. Y. Shi, M. Ren and I. Zhitomirsky, *ACS Sustainable Chem. Eng.*, 2014, **2**, 1289.
23. H. Wang, D. S. Zhang, T. T. Yan, X. R. Wen, L. Y. Shi and J. P. Zhang, *J. Mater. Chem.*, 2012, **22**, 23745.
24. H. Wang, L. Y. Shi, T. T. Yan, J. P. Zhang, Q. D. Zhong and D. S. Zhang, *J. Mater. Chem. A*, 2014, **2**, 4739.
25. X. R. Wen, D. S. Zhang, T. T. Yan, J. P. Zhang and L. Y. Shi, *J. Mater. Chem. A*, 2013, **1**, 12334.
26. P. Xu, J. E. Drewes, D. Heil and G. Wang, *Water Res.*, 2008, **42**, 2605.
27. M. Haro, G. Rasines, C. Macias and C. O. Ania, *Carbon*, 2011, **49**, 3723.
28. D. Zhang, X. Wen, L. Shi, T. Yan and J. Zhang, *Nanoscale*, 2012, **4**, 5440.
29. Z. Peng, D. S. Zhang, L. Y. Shi and T. T. Yan, *J. Mater. Chem.*, 2012, **22**, 6603.
30. H. B. Zhang, W. G. Zheng, Q. Y. Yan, Z. G. Jiang and Z. Z. Yu, *Carbon*, 2012, **50**, 5117.
31. F. Y. Yuan, H. B. Zhang, X. F. Li, H. L. Ma, X. Z. Li and Z. Z. Yu, *Carbon*, 2014, **68**, 653.
32. R. K. Upadhyay, N. Soin and S. S. Roy, *RSC Adv.*, 2014, **4**, 3823.
33. H. Bi, S. R. Sun, F. Q. Huang, X. M. Xie and M. H. Jiang, *J. Mater. Chem.*, 2012, **22**, 411.
34. Z. H. Ni, T. Yu, Y. H. Lu, Y. Y. Wang, Y. P. Feng and Z. X. Shen, *ACS nano*, 2008, **2**, 2301.
35. J. H. Li, L. Y. Niu, Z. J. Zheng and F. Yan, *Adv. Mater.*, 2014, **26**, 5239.
36. Y. T. Liu, Q. P. Feng, X. M. Xie and X. Y. Ye, *Carbon*, 2011, **49**, 3371.
37. X. Yang, L. Zhang, F. Zhang, T. F. Zhang, Y. Huang and Y. S. Chen, *Carbon*, 2014, **72**, 381.
38. H. J. Yin, S. L. Zhao, J. W. Wan, H. J. Tang, L. C. Chang, L. He, H. J. Zhao, Y. Gao and Z. Y. Tang, *Adv. Mater.*, 2013, **25**, 6270.
39. H. B. Li, T. Lu, L. K. Pan, Y. Zhang and Z. Sun, *J. Mater. Chem.*, 2009, **19**, 6773.
40. W. Fan, Y. Y. Xia, W. W. Tjiu, P. K. Pallathadka, C. B. He and T. X. Liu, *J. Power Sources*, 2013, **243**, 973.
41. Y. H. Lu, F. Zhang, T. F. Zhang, K. Leng, Y. Huang, X. Yang, Y. F. Ma, M. J. Zhang and Y. S. Chen, *Carbon*, 2013, **63**, 508.
42. W. Fan, C. Zhang, W. W. Tjiu, K. P. Pramoda, C. B. He and T. X. Liu, *ACS Appl. Mater. Inter.*, 2013, **5**, 3382.
43. H. H. Chang, C. K. Chang, Y. C. Tsai and C. S. Liao, *Carbon*, 2012, **50**, 2331.
44. Y. T. Liu, M. Dang, X. M. Xie, Z. F. Wang and X. Y. Ye, *J. Mater. Chem.*, 2011, **21**, 18723.
45. A. Davies, P. Audette, B. Farrow, F. Hassan, Z. W. Chen, J. Y. Choi and A. P. Yu, *J. Phys. Chem. C*, 2011, **115**, 17612.
46. C. Bora and S. K. Dolui, *Polymer*, 2012, **53**, 923.
47. M. K. Liu, W. W. Tjiu, J. S. Pan, C. Zhang, W. Gao and T. X. Liu, *Nanoscale*, 2014, **6**, 4233.
48. E. Raymundo-Piñero, V. Khomenko, E. Frackowiak and F. Béguin, *J. Electrochem. Soc.*, 2005, **152**, A229.
49. Z. Fan, J. H. Chen, M. Y. Wang, K. Z. Cui, H. H. Zhou and Y. F. Kuang, *Diam. Relat. Mate.*, 2006, **15**, 1478.
50. Y. K. Zhou, B. L. He, F. B. Zhang and H. L. Li, *J. Solid State Eletrochem.*, 2004, **8**, 482.
51. C. Y. Lee, H. M. Tsai, H. J. Chuang, S. Y. Li, L. P. and T. Y. Tseng, *J. Electrochem. Soc.*, 2005, **152**, A716.
52. J. Yan, Z. J. Fan, T. Wei, W. Z. Qian, M. L. Zhang and F. Wei, *Carbon*, 2010, **48**, 3825.
53. F. Zhang, F. Xiao, Z. H. Dong and W. Shi, *Electrochim. Acta*, 2013, **114**, 125.
54. H. Zhou, T. Ni, X. T. Qing, X. X. Yue, G. Li and Y. Lu, *RSC Adv.*, 2014, **4**, 4134.
55. X. Y. Gu, Y. Ning, Y. Yang and C. Y. Wang, *RSC Adv.*, 2014, **4**, 3211.
56. Z. H. Dong, Y. L. Wei, W. Shi and G. A. Zhang, *Mater. Chem. Phys.*, 2011, **131**, 529.
57. R. K. Sharma, A. Karakoti, S. Seal and L. Zhai, *J. Power Sources*, 2010, **195**, 1256.
58. P. Li, Y. Yang, E. Shi, Q. Shen, Y. Shang, S. Wu, J. Wei, K. Wang, H. Zhu, Q. Yuan, A. Cao and D. Wu, *ACS Appl. Mater. Inter.*, 2014, **6**, 5228.
59. H. Zhou, T. Ni, X. T. Qing, X. X. Yue, G. Li and Y. Lu, *RSC Adv.*, 2014, **4**, 4134.
60. D. S. Zhang, T. T. Yan, L. Y. Shi, Z. Peng, X. R. Wen and J. P. Zhang, *J. Mater. Chem.*, 2012, **22**, 14696.
61. Y. J. Kim and J. H. Choi, *Water Res.*, 2010, **44**, 990.
62. B. P. Jia and L. Zou, *Carbon*, 2012, **50**, 2315.
63. J. Yan, Z. J. Fan, T. Wei, W. Z. Qian, M. L. Zhang and F. Wei, *Carbon*, 2010, **48**, 3825.
64. B. Mu, W. B. Zhang, S. J. Shao and A. Q. Wang, *Phys. Chem. Chem. Phys.*, 2014, **16**, 7872.
65. K. V. Kalpana and R. K. Selvan, *J. Appl. Electrochem.*, 2012, **42**, 463.
66. N. Xiao, D. M. Lau, W. H. Shi, J. X. Zhu, X. C. Dong, H. H. Hng and Q. Y. Yan, *Carbon*, 2013, **57**, 184.
67. L. Zhang and G. Q. Shi, *J. Phys. Chem. C*, 2011, **115**, 17206.
68. Y. Zhao, J. Liu, Y. Hu, H. H. Cheng, C. G. Hu, C. C. Jiang, L. Jiang, A. Q. Cao and L. T. Qu, *Adv. Mater.*, 2013, **25**, 591.
69. S. Sahoo, G. Karthikeyan, G. C. Nayak and C. K. Das, *Synthetic Met.*, 2011, **161**, 1713.
70. C. Kim, J. Lee, S. Kim and J. Yoon, *Desalination*, 2014, **342**, 70.
71. H. Wang, D. S. Zhang, T. T. Yan, X. R. Wen, J. P. Zhang, L. Y. Shi and Q. D. Zhong, *J. Mater. Chem. A*, 2013, **1**, 11778.
72. S. Sahoo, S. Dhibar, G. Hatui, P. Bhattacharya and C. K. Das, *Polymer*, 2013, **54**, 1033.
73. Z. Yu and J. Thomas, *Adv. Mater.*, 2014, **26**, 4279.
74. M. C. Zafra, P. Lavela, G. Rasines, C. Mac ás, J. L. Tirado and C. O. Ania, *Electrochim. Acta*, 2014, **135**, 208.
75. A. G. El-Deen, N. A. M. Barakat and H. Y. Kim, *Desalination*, 2014, **344**, 289.
76. K. Laxman, M. T. Myint, H. Bourdoucen and J. Dutta, *ACS Appl. Mater. Inter.*, 2014, **6**, 10113.
77. H. B. Li, L. Zou, L. K. Pan and Z. Sun, *Environ. Sci. Technol.*, 2010, **44**, 8692.
78. X. Y. Gu, Y. Yang, Y. Hu, M. Hu, J. Huang and C. Y. Wang, *RSC Adv.*, 2014, **4**, 63189.
79. S. Jeon, H. Park, J. Yeo, S. C. Yang, C. H. Cho, M. H. Han and D. K. Kim, *Energ. Environ. Sci.*, 2013, **6**, 1471.
80. H. B. Li, S. Liang, J. Li and L. J. He, *J. Mater. Chem. A*, 2013, **1**, 6335.